physica status solidi rrl
www.pss-rapid.com

Wave-Vector-Dependent Raman Scattering from Coupled Plasmon–Longitudinal Optical Phonon Modes and Fano Resonance in *n*-type Scandium Nitride

*Krishna Chand Maurya, Bidesh Biswas, Magnus Garbrecht, and Bivas Saha**

Raman scattering from coupled plasmon–longitudinal optical (LO) phonon modes in polar semiconductors is an effective tool to determine electronic properties, such as carrier concentration, mobility, carrier freeze-out, relaxation times, etc., as well as to understand different types of electron (hole)–phonon interactions. The physics of such coupling mechanism traditionally utilizes the Drude dielectric permittivity that predicts an increase in coupled plasmon–LO phonon mode (LPP+) frequencies with an increase in carrier concentrations. Herein, it is demonstrated that for *n*-type epitaxial scandium nitride (ScN) thin films, the frequencies of the coupled plasmon–LO phonon Raman modes exhibit red-shift with increasing carrier concentrations, which is contrary to the predictions from the Drude theory. Utilizing the generalized Lindhard dielectric function that considers both the frequency and wave-vector components of free-electron plasma, it is demonstrated that such a decrease in the frequencies of the coupled plasmon–LO phonon mode in Raman spectra is related to the non-conserved wave vectors due to inelastic scattering from magnesium (Mg) impurities. Modeling of the experimental Raman line shape, intensity, and frequencies illustrates that the wave-vector dependence of the coupled modes decreases with increasing electron concentrations. An asymmetric broadening of LO Raman modes is observed in films having large electron concentrations (>10^{20} cm^{-3}) that are explained by Fano resonance.

In heavily doped semiconductors, the free carrier plasma interacts strongly with the longitudinal optical (LO) lattice vibration or phonons via their macroscopic electric fields.[1–4] The dispersion relation of such coupled plasmon–LO phonon modes, denoted by LPP $\pm$ ($\vec{q}$), is traditionally explained by the Drude dielectric function[5,6] model of the free carrier plasma and has been studied for long using Raman spectroscopy.[7] For small wave vector ($\vec{q} \cong 0$) (nominal momentum transfer of the incident and scattered photons), the frequency of the LPP$^-$ mode for lower carrier concentrations is less than that of the transverse optical (TO) phonon frequency and approaches to that of the TO phonon frequency at higher carrier concentration, whereas the frequency of the LPP$^+$ mode is higher than that of the LO phonon frequency and increases with increasing carrier concentrations.[3,4] The LPP$^+$ mode exhibits phonon-like characteristics at lower carrier concentrations and becomes plasmon-like at higher concentrations, provided that the plasmon and phonon damping constants are small, i.e., the system is not overdamped.[3,4]

Since the first experimental observation of such effects in *n*-type GaAs in the 1960s,[8] Raman scattering of such coupled plasmon–LO phonon modes has become an alternative optical tool to determine electron and hole concentrations, plasmon and phonon relaxation times, carrier mobility, carrier freeze-outs, etc. in several elemental and compound semiconductors,[9–12] such as in *n*-type GaN, InN, SiC, graphene, etc. The utility of this technique is particularly important for the determination of the electrical properties of semiconductors as it is not necessary to establish ohmic contacts (which could be difficult to achieve, especially for semiconductor with low carrier concentrations) and since the local resolution of this technique is high compared with the electrical measurements, limited only by the necessity of focusing the laser beam.[3] Similarly, Raman scattering of the coupled mode has also been useful as a nondestructive optical method for the determination of the electronic properties for nanostructured materials, where electrical measurement is extremely challenging to perform,[13–16] such as on nanowall networks, nanowires, nanoplates, etc.

K. C. Maurya, B. Biswas, Dr. B. Saha
International Centre for Materials Science
Jawaharlal Nehru Centre for Advanced Scientific Research
Jakkur, Bangalore 560064, India
E-mail: bsaha@jncasr.ac.in, bivas.mat@gmail.com

K. C. Maurya, B. Biswas, Dr. B. Saha
Chemistry and Physics of Materials Unit
Jawaharlal Nehru Centre for Advanced Scientific Research
Jakkur, Bangalore 560064, India

K. C. Maurya, B. Biswas, Dr. B. Saha
School of Advanced Materials
Jawaharlal Nehru Centre for Advanced Scientific Research
Jakkur, Bangalore 560064, India

Dr. M. Garbrecht
Australian Centre for Microscopy and Microanalysis
The University of Sydney
Sydney, NSW 2006, Australia

The ORCID identification number(s) for the author(s) of this article can be found under https://doi.org/10.1002/pssr.201900196.

DOI: 10.1002/pssr.201900196

Coupled plasmon–LO phonon modes of large wave vectors ($\vec{q}$) have also been observed in several semiconductors, such as in heavily doped *p*-type C and Ge-doped GaAs,[17,18] *n*-type Si-doped GaN nanowires,[16] *n*-type Al-doped ZnSe,[19] etc. The large wave-vector transfer ($\vec{q}$) arises from the nonconservation of wave vector due to scattering by ionized impurities and affects the line shapes of the coupled modes, causing a decrease in the frequencies of the LO-like modes with increasing carrier concentrations.[16–19] Therefore, along with the knowledge of electronic properties, Raman scattering of the coupled modes can also be effective to determine various carrier scattering mechanism and carrier dynamics studies.

Scandium nitride (ScN) is a group 3 rocksalt indirect bandgap semiconductor[20–22] and has attracted significant interest in recent years for its potential applications in thermoelectricity and thermionic energy conversion,[23,24] solid-state lighting for reducing threading dislocation densities of GaN epi-layers[25,26], and as a semiconducting component for epitaxial single crystalline metal/semiconductor superlattice growth.[27,28] Sputter-deposited[24] ScN thin films are heavily doped with *n*-type carriers having a room temperature carrier concentration of (2–4) $\times 10^{20}$ cm^{-3} due to the presence of oxygen (O_N) as impurities and possible nitrogen vacancies (V_N). Such high carrier concentrations and favorable indirect bandgap ($\Gamma - X$) of 0.9 eV in ScN lead to a large thermoelectric power factor[24] of 3.5×10^{-3} $W\,mK^{-2}$ at high temperatures (800 K), which can be utilized for designing efficient waste heat to electrical energy conversion devices. Moreover, due to its rocksalt crystal structure and a direct bandgap of 2.2 eV, ScN can also be utilized for alloying with other wurtzite nitride semiconductors for bandgap engineering.[29] For widespread electronic applications, it is also important to reduce its carrier concentrations and develop *p*-type ScN thin films.[30–33] Hole doping by the incorporation of Mg_xN_y in ScN has led to reduced carrier concentrations in ScN, and *p*-type epitaxial $Sc_{1-x}Mg_xN$ thin films with high hole concentrations (2×10^{20} cm^{-3}) have been developed. Recent synchrotron and first-principles modeling analyses have also shown that the rigid-band electronic structure of ScN remains unchanged with respect to the *n*-to-*p*-type carrier transitions, without the presence of any mid-gap states,[34] as well as unchanged valence and conduction band edges that are important for electronic transport.

Due to its rocksalt crystal structure, the first-order Raman scattering in ScN is symmetry forbidden. However, the presence of defects relaxes the *q*-selection rules, and a weighted one-phonon densities of phonon states were obtained in Raman measurement for ScN films, which showed a broad acoustic phonon peak at ≈420 cm^{-1} and an optical phonon mode at ≈677 cm^{-1} that is assigned to the LO phonon from density functional perturbation theory calculations of the phonon dispersion spectrum.[35–38] Recently, inelastic X-ray scattering studies[39] on epitaxial ScN thin film have been used to determine the phonon lifetimes as a function of momentum that exhibited a short lifetime of 0.21 ps for the highest energy phonon mode around the zone -center. The inelastic X-ray scattering studies[39] have also demonstrated that the LO phonon mode at the Γ -point of the Brillouin zone has an energy of ≈84 meV (corresponding to 677 cm^{-1}), whereas the LO phonon mode energy at the L-point of the Brillouin zone has ≈80 meV (corresponding to 645 cm^{-1}). Hence, the Raman mode of ScN at 677 cm^{-1} was assigned to the LO mode at the -point of the Brillouin zone. Similarly, inelastic X-ray scattering[39] also demonstrated that the TO phonon mode at the Γ -point of the Brillouin zone exhibited an energy of ≈42 meV, corresponding to ≈339 cm^{-1}, which was subsequently used for a modeling analysis. Therefore, the electronic and vibrational properties of ScN have been an important research topic in recent years, and understanding the carrier scattering mechanism and carrier dynamics would help further develop ScN-based efficient electronic and thermoelectric devices. In this letter, wave-vector-dependent Raman scattering from coupled plasmon–LO phonon modes in *n*-type ScN is demonstrated. Nonconservation of the wave vector due to inelastic scattering from impurities leads to a red-shift of the coupled mode with increasing electron concentrations in magnesium (Mg)-doped ScN thin films. Asymmetric line shapes at large electron concentrations are also observed due to Fano resonance[40] from the coupling of phonon scattering and a Raman-active continuum of electronic excitations.

Epitaxial-undoped ScN and $Sc_{1-x}Mg_xN$ thin films were deposited on (001) MgO substrates with high-vacuum DC-magnetron cosputtering (see Supporting Information for details). The Mg-doping concentrations inside ScN were increased to achieve electron concentrations ranging from the highest 2.6×10^{20} cm^{-3} for undoped ScN to the lowest 1.6×10^{18} cm^{-3} for $Sc_{0.975}Mg_{0.025}N$ thin film. Further increase in Mg concentrations leads to an *n*-to-*p*-type carrier transition,[30,31] as the unintentional dopant and impurity concentrations were very low and remained unchanged with respect to the incorporation of Mg dopants in ScN. However, for ScN thin films that contained a large amount (≈9 atm%) of oxygen (O_N) as an impurity, the films retained its *n*-type carrier nature even with Mg_xN_y incorporations.[41] An X-ray diffraction (XRD) analysis showed that all films grow with 002 orientations on MgO substrates with *c*-axis lattice constants that are similar to the lattice parameter of undoped ScN (**Figure 1**a). The full-width-at-the-half-maxima (FWHM) of the ω-scan (rocking curve) ranged between 0.7° and 1° (Figure 1b), which represented textured nominally single-crystalline film growth. A transmission electron microscopy (TEM) analysis was performed with the Australian Centre for Microscopy & Microanalysis image- and probe-corrected and monochromated FEI Themis-Z 60–300 kV instrument. TEM samples were prepared by the focused ion beam using the lift-out technique. TEM micrographs show clear and well-defined $Sc_{1-x}Mg_xN$/MgO interfaces (Figure 1b) with cube-on-cube crystal growth having an epitaxial relationship of $Sc_{1-x}Mg_xN$ [001](001) || MgO [001](001) (Figure 1b). Due to ≈7% lattice mismatch between ScN and MgO substrates, some misfit dislocations were observed at the $Sc_{1-x}Mg_xN$/MgO interfaces. Microscopy imaging also showed that Mg incorporation in ScN creates a homogeneous solid solution, without any sign of Mg precipitation, secondary phase formation, or phase separation (see Supporting Information for details).

Raman spectroscopy of undoped ScN and $Sc_{1-x}Mg_xN$ thin films was performed in backscattering geometry with a Horiba Raman spectrometer at room temperature with two different incident photon energies, 2.3 eV (λ= 540 nm) and 1.96 eV (λ = 630 nm). Undoped ScN thin films exhibit a clear and distinct Raman mode at 677 cm^{-1} consistent with previous reports.[35,36] Similarly, though a broad acoustic peak was visible in the

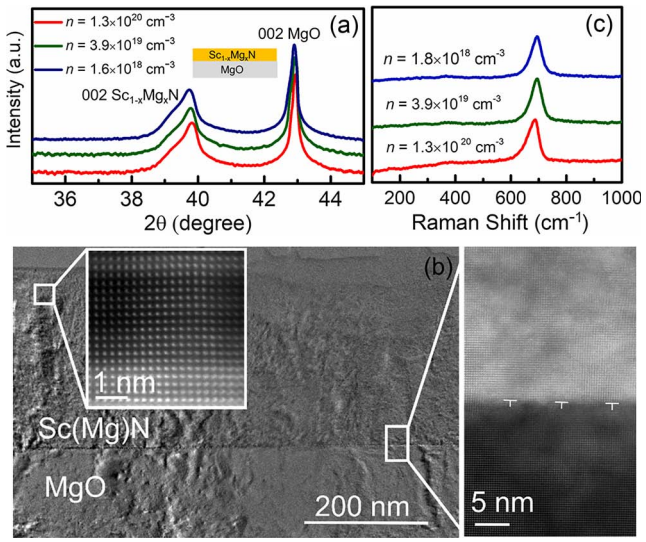

Figure 1. a) XRD spectra of three representative $Sc_{1-x}Mg_xN$ thin films are presented. The alloy films grow with 002 orientation on the (001) MgO substrate. b) HRTEM micrograph of $Sc_{0.982}Mg_{0.018}N$/MgO is presented. The insets show an atomic resolution image of the $Sc_{0.982}Mg_{0.018}N$ layer demonstrating the epitaxial crystal growth. The atomically resolved STEM micrograph of the interface shows misfit dislocations due to the lattice mismatch. c) Raman spectrum of three representative films having different carrier concentrations and measured with an incident energy of 2.3 eV are presented.

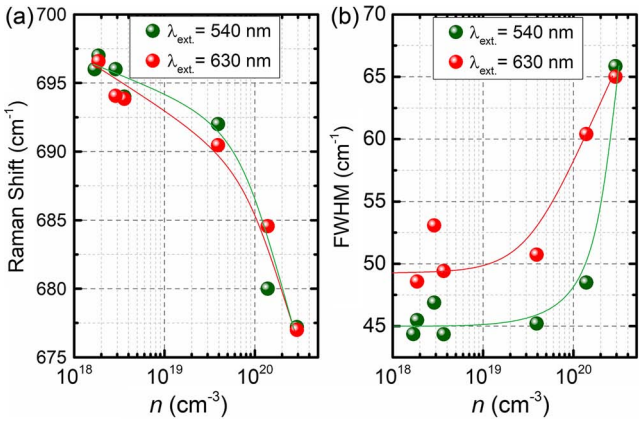

Figure 2. a) Coupled plasmon–LO phonon peak in Raman scattering spectrum of $Sc_{1-x}Mg_xN$ thin films are presented as a function of electron concentration (n) for two different incident light wavelengths ($\lambda = 540$ nm) and ($\lambda = 630$ nm). b) The FWHM of the coupled modes are presented as a function of n. The frequencies of the coupled mode were found to decrease with an increase in the electron concentration due to the nonconservation of wave vectors. The lines drawn through the data are meant to guide the eye.

spectrum, deciphering it into LA and TA modes was not possible. All other $Sc_{1-x}Mg_xN$ thin films exhibited (Figure 1c) well pronounced Raman mode with frequencies that are close to that of the undoped ScN's Raman peak. The acoustic phonon modes were much diminished in Mg-doped ScN films in comparison with the spectrum for undoped ScN. The peak position of the Raman mode decreased with increasing carrier concentrations from $696\,\mathrm{cm}^{-1}$ for $n_e = 1.6 \times 10^{18}\,\mathrm{cm}^{-3}$ to $677\,\mathrm{cm}^{-1}$ for $n_e = 2.6 \times 10^{20}\,\mathrm{cm}^{-3}$ for both of the incident laser photon energies (**Figure 2**a). Concomitant with the decrease in frequencies, the FWHM of the phonon mode also increased from ≈45 to ≈65 cm^{-1} ($\lambda = 540$ nm) with the same increase in the electron concentration inside the films (Figure 2b).

As mentioned before, the physical mechanism of coupled plasmon–LO phonon mode that considers the Drude model for the dielectric permittivity of the free-electron plasma predicts an increase in the frequencies of the LPP^+ coupled mode with an increase in the electron concentrations[1,2] (see Supporting Information for detailed model). Dielectric permittivity in the Drude model is a function of the plasma frequency and useful for describing plasmon–LO phonon coupling when the wave-vector transfer is negligible ($\vec{q} \cong 0$). However, due to the presence of impurities (doping, alloying, or the presence of unwanted atomic species from crystal growth), the incident photons can transfer momentum to the coupled plasmon–LO phonon modes through inelastic scattering that results in the nonconservatized large wave vector ($\vec{q} \gg \vec{q}_{TF}$, with $\vec{q}_{TF}$ being Thomas–Fermi wave vector) and fundamentally alter the coupling mechanisms. To capture the physics of such nonconserved wave vector in plasmon–LO phonon coupling, the experimental Raman spectra (frequency, line shape, and intensity) were modeled and fitted with the generalized Lindhard model[42,43] of the dielectric function that considers both the frequency and wave-vector components of free-electron plasma with two different scattering mechanisms. The Raman line shape is expressed by Equation (1) as

$$I = A \times B(\omega) \times \mathrm{Im}\left(-\varepsilon_{\mathrm{total}}^{-1}\right) \tag{1}$$

where A is a constant, B is a frequency-dependent parameter that also depends on scattering mechanism, and $\varepsilon_{\mathrm{total}}$ is the total dielectric function, expressed in Equation (2) as

$$\varepsilon_{\mathrm{total}} = \varepsilon_{\infty} + \varepsilon_{\mathrm{phonon}} + \varepsilon_{\mathrm{plasmon}} \tag{2}$$

where ε_{∞} is the high-frequency dielectric constant, whereas $\varepsilon_{\mathrm{phonon}}$ and $\varepsilon_{\mathrm{plasmon}}$ are the dielectric function of phonon and plasmon, respectively. The phonon contribution of the dielectric permittivity is expressed in Equation (3) as

$$\varepsilon_{\mathrm{phonon}} = \frac{{\omega_{\mathrm{LO}}}^2 - {\omega_{\mathrm{TO}}}^2}{{\omega_{\mathrm{TO}}}^2 - \omega^2 - i \times \omega \times \gamma} \tag{3}$$

where $\omega_{\mathrm{LO}}, \omega_{\mathrm{TO}}$ are the LO and TO phonon frequencies, respectively, and γ is the phonon damping constant.

The Lindhard dielectric constant of the free-electron plasma is expressed in Equation (4) as

$$\varepsilon_{\mathrm{plasmon}}(q,\omega) = \varepsilon_{\infty} - \frac{e^2}{q^2}\int d^3k \frac{f(k+q) - f(k)}{E(k+q) - E(k) - \hbar(\omega + i \times s)} \tag{4}$$

where $f(k)$ is the Fermi–Dirac distribution function for electrons in thermodynamic equilibrium, q ($q = q' - q''$, where q' and q'' are the wave vector of the incident and scattered photon, respectively) is the wave vector, and s is a positive infinitesimal constant. $B(\omega)$ in Equation (1) depends on phonon frequencies and

exhibits different expressions for 1) deformation potential scattering and electro-optical scattering and 2) scattering due to density fluctuation of the free carriers (see Supporting Information for a detailed discussion). Based on the previous reports[27–31,39] of ScN (see Supporting Information for more details), a high-frequency dielectric constant (ε_∞) of 12.3, ω_{LO}, ω_{TO} of 677 and 339 cm^{-1}, respectively, and an effective mass of $m_{eff} = 0.39\, m_0$ (where m_0 is the mass of a free electron) were used for the modeling to extract the damping constants, as well as the momentum transfer between the incident and scattered light.

The theoretically modeled Raman spectra of $Sc_{1-x}Mg_xN$ thin film with $n_e = 1.86 \times 10^{18}$ cm^{-3} (representative for all thin film samples having $n_e < 10^{20}$ cm^{-3}) match well with experimental measurements (presented in **Figure 3**) for the two different coupling mechanisms at two different incident laser wavelengths. Fittings based on the deformation potential scattering and electro-optical scattering mechanism suggest that the phonon damping constants increase monotonically with increasing carrier concentrations (see **Figure 4**a) that are consistent with the experimentally observed FWHM of the Raman spectra. However, the plasmon damping constants were found to remain nearly invariant. On the contrary, fittings of the Raman spectrum with scattering due to density fluctuation of free carrier show that both the plasmon and phonon damping constants exhibit dependence on the carrier concentration, albeit any monotonic trends. Importantly, both of the mechanisms exhibit (see Figure 4a) decrease in the wave-vector (q) transfer from the incident to scattered photon with the increase in the electron concentration due to the decreasing amount of impurity (Mg) concentrations in the film, also observed[2,4] in p-doped GaAs.

The coupled plasmon–LO phonon Raman models, however, were unable to capture the asymmetric broadening of the Raman line shape for films having large electron concentrations ($>10^{20}$ cm^{-3}), since such asymmetry in Raman line shapes arises due to Fano-like[40,44–46] coherent discrete–continuum interaction between the phonon scattering and a Raman-active continuum of electronic excitations from the filled to empty conduction band states. Such electronic excitations are known to occur when the doping level in semiconductor is sufficiently high that leads to partial filling of the conduction band states, and the energy continuum of the transitions overlaps with the energy of the discrete Raman-active optical phonon with the same symmetry, and an interference between the phonon and the electronic transitions takes place. These asymmetric Fano-like Raman line shapes have been observed in heavily doped n- and p-type Si,[44,46] p-type Ge,[45] p-type GaAs,[45] etc., and though they are infrared forbidden but are Raman active. For ScN thin films, previous first-principles and Boltzmann transport modeling analyses[31] of the thermoelectric properties have demonstrated that for an

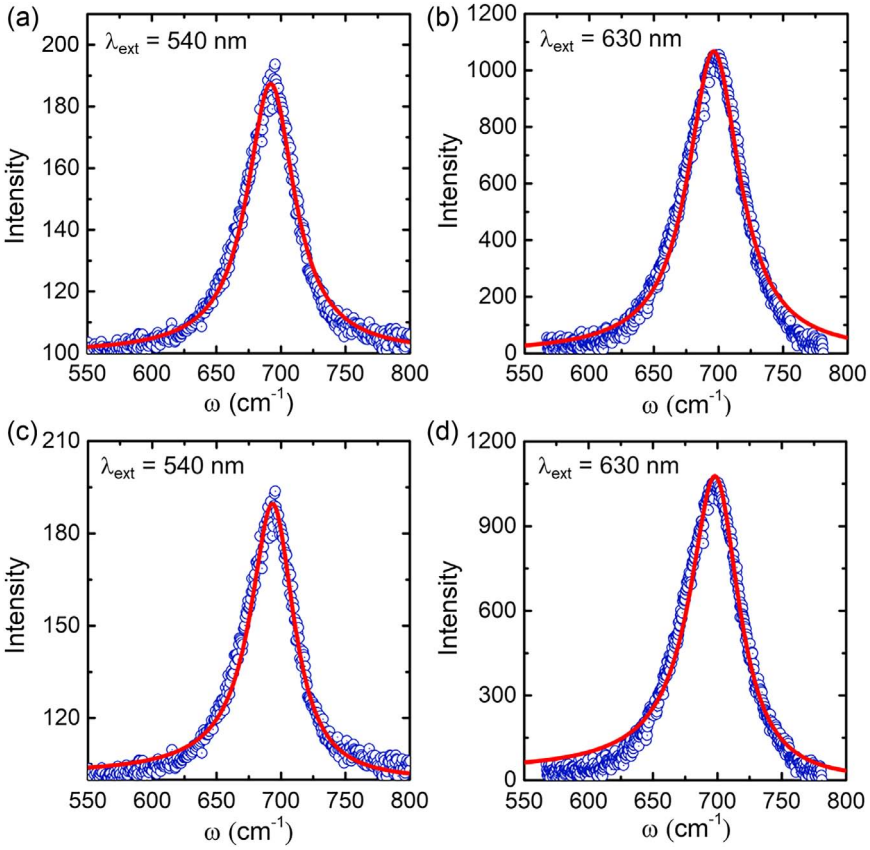

Figure 3. Experimental (blue circles with a dot) and theoretically modelled (red line) Raman shift ($\omega(cm^{-1})$) of $Sc_{1-x}Mg_xN$ thin film with $n_e = 1.86 \times 10^{18}$ cm^{-3} is presented using two incident laser wavelengths ($\lambda = 540$ nm) and ($\lambda = 630$ nm), for the two different scattering mechanisms: a,b) deformation potential scattering and electro-optical scattering and c,d) scattering due to density fluctuation of the free carriers.

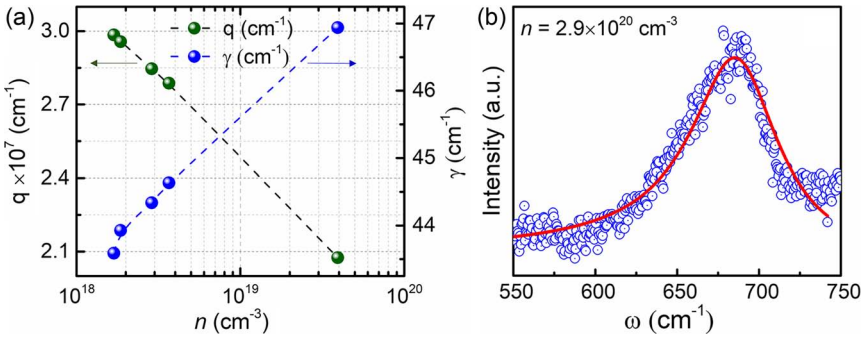

Figure 4. a) Wave-vector transfer (q) and phonon damping constants are presented as a function of the carrier concentrations for an incident laser wavelength of 540 nm (an incident laser wavelength of 630 nm also exhibits similar behavior). The extent of wave-vector transfer (q) was found to decrease with increasing carrier concentrations. The lines drawn through the data are meant to guide the eye. b) Raman shift ($\omega(\text{cm}^{-1})$) for undoped ScN thin film having the highest electron concentration is presented. The plasmon–LO phonon coupling model does not fit the experimental Raman spectrum for such large carrier concentrations and suggests an uncoupled LO phonon mode. The asymmetry in Raman mode was a result of Fano resonance arising due to the coherent discrete-continuum interactions between the phonon scattering and a Raman-active continuum of electronic excitations.

electron concentration greater than ≈(3–4) × 10^{19} cm^{-3}, the Fermi level shifts to the conduction band. For an as-deposited ScN thin films having $n_e = 2.6 \times 10^{20}\,\text{cm}^{-3}$, the Fermi level should be located at ≈60–100 meV above the conduction band edge (see Supporting Information). The presence of electrons in the conduction band valleys allows interband electronic transitions, and as the energy of the discrete LO phonon state, which has the same symmetry as the interband transitions, falls within the continuum, interference between the discrete state and the continuum takes place. These interference has been treated by Fano[40] and is the origin for the asymmetric line shapes in Raman spectra (see Figure 4b).

Utilizing the Fano resonance mode, the Raman scattering line shape for high electron concentrations was modeled (Equation (5))

$$I = A \times \frac{(fg + \omega - \omega_0)^2}{(\omega - \omega_0)^2 + g^2} \tag{5}$$

where ω_0 and g denote the position and width of the resonance, respectively, f is the Fano parameter, which describes the degree of asymmetry, and A is a constant. Values of f are positive for a hole and negative for an electron. The fitting yielded Fano parameter of −12.6 for $n_e = 2.92 \times 10^{20}\,\text{cm}^{-3}$ and −7.3 for $n_e = 1.39 \times 10^{20}\,\text{cm}^{-3}$ that is consistent with the physical Fano resonance model. In addition to the asymmetric line shape, Fano-like resonance[44–46] also introduces a small shift in the position of phonon frequencies that may be described as changes in the real part of the self-energy due to phonon deformation-potential interaction with the free electron in the conduction band.[44,46] Experimentally observed small shift in the peak frequency (Figure 2a) from 685 to 677 cm^{-1} for $\lambda = 630$ nm, and from 680 to 677 cm^{-1} for $\lambda = 540$ nm, with a decrease in the electron concentration from $n_e = 1.39 \times 10^{20}$ to $2.92 \times 10^{20}\,\text{cm}^{-3}$ are concluded to be due to the Fano resonance effect.

In conclusion, wave-vector (q) nonconservation in coupled plasmon–LO phonon modes in epitaxial ScN thin films exhibited Stokes Raman scattering and demonstrated a red-shift of the coupled mode frequencies with increasing carrier concentrations. Lindhard dielectric function that takes into account both the frequency and wave-vector components of free-electron plasma is utilized to model the experimental Raman spectra along with the deformation potential scattering and electro-optical scattering, as well as scattering due to density fluctuation of the free carriers. The wave-vector transfer ($\vec{q}$) was found to decrease with decreasing Mg impurity concentrations and eventually led to LO phonon modes in high carrier concentrations that couple with the Raman-active continuum of electronic excitations from the filled to empty conduction band states exhibiting asymmetric Fano resonance. Findings presented in this study are important not only for understanding the plasmon–phonon coupling and scattering mechanism in ScN but also will help design ScN-based thermal and thermoelectric devices with improved efficiencies.

Supporting Information

Supporting Information is available from the Wiley Online Library or from the author.

Acknowledgements

K.C.M., B.B., and B.S. acknowledge financial support from the International Centre for Materials Science (ICMS) of Jawaharlal Nehru Center for Advanced Scientific Research (JNCASR). B.B. and B.S. acknowledge B.S. Vasudeb for assistance with the Raman Measurements. K.C.M. and B.S. acknowledge Center for Computational Materials Science (CCMS) in JNCASR for support. We acknowledge support in specialized TEM sample preparation at the Karlsruhe Nano Micro Facility (Project ID: 2015–015-010151) by M.H. Fahwey and V.S.K. Chakravadhanula. All authors acknowledge Sanjay Nayak for helpful discussions.

Conflict of Interest

The authors declare no conflict of interest.

Keywords

scandium nitride (ScN), Raman scattering, wave-vector dependent Raman scattering, coupled plasmon–phonon mode, Fano resonance

Received: April 3, 2019
Revised: May 7, 2019
Published online:

[1] B. B. Vagra, *Phys. Rev.* **1965**, *8*, 1896.
[2] M. Cardona, G. Guntherodt, *Light Scattering in Solids IV*, Springer-Verlag, Berlin/New York **1984**.
[3] G. Irmer, V. V. Toporov, B. H. Bairamov, J. Monecke, *Phys. Status Solidi B* **1983**, *119*, 595.
[4] D. Olego, M. Cardona, *Phys. Rev. B* **1981**, *24*, 7217.
[5] N. W. Ashcroft, N. D. Mermin, *Solid-State Physics*, Saunders College, Philadelphia **1976**. Appendix N. 2010.
[6] L. Genzel, T. P. Martin, Z. Kreibig, *Physica B* **1975**, *21*, 339.
[7] D. A. Long, *Raman Spectroscopy*, McGraw-Hill, New York **1977**.
[8] A. Mooradian, G. B. Wright, *Phys. Rev. Lett.* **1966**, *16*, 999.
[9] T. Kozawa, T. Kachi, H. Kano, Y. Taga, M. Hashimoto, *J. Appl. Phys.* **1993**, *75*, 1098.
[10] R. Cuscó, J. Ibáñez, E. Alarcón-lladó, L. Artús, *Phys. Rev. B* **2009**, *79*, 155210.
[11] M. V. Klein, B. N. Ganguly, P. J. Colwell, *Phys. Rev. B* **1972**, *6*, 2380.
[12] E. H. Hwang, R. Sensarma, S. Das Sarma, *Phys. Rev. B* **2010**, *82*, 195406.
[13] R. Kumar, S. Nayak, S. M. Shivaprasad, *Spectroscopic Signatures of Native Charge Compensation in Mg Doped GaN Nanorods*, arXiv:1807.01121, **2018**.
[14] S. S. R. Challa Kumar, *Raman Spectroscopy for Nanomaterials Characterization*, Springer, Berlin, Heidelberg **2012**, ISBN 978-3-642-20620-7.
[15] K. Jeganathan, R. K. Debnath, R. Meijers, T. Stoica, R. Calarco, D. Grützmacher, H. Lüth, *J. Appl. Phys.* **2009**, *105*, 123707.
[16] E. Rozas-Jiménez, A. Cros, S. Murcia-Mascarós, Z. Fang, B. Daudin, *Mater. Sci. Semicond. Process.* **2016**, *55*, 63.
[17] R. A. Munoz-Hernandez, S. Jimenez-Sandoval, G. Torres-Delgado, C. Roch, X. K. Chen, J. C. Irwin, *J. Appl. Phys.* **1996**, *80*, 2388
[18] M. Seon, M. Holtz, W. M. Duncan, T. S. Kim, *J. Appl. Phys.* **1999**, *85*, 7224.
[19] H. Yugami, S. Nakashima, K. Sakai, H. Kojima, M. Hangyo, A. Mitsuishi, *J. Phys. Soc. Jpn*. **1987**, *56*, 1881.
[20] B. Biswas, B. Saha, *Phys. Rev. Mater.* **2019**, *3*, 020301.
[21] JP Dismukes, *J. Cryst. Growth* **1972**, *13*, 365.
[22] D. Gall, I. Petrov, N. Hellgren, L. Hultman, J. E. Sundgren, J. E. Greene, *J. Appl. Phys.* **1998**, *84*, 6034.
[23] S. Kerdsongpanya, N. Van Nong, N. Pryds, A. Žukauskaite, J. Jensen, J. Birch, J. Lu, L. Hultman, G. Wingqvist, P. Eklund, *Appl. Phys. Lett.* **2011**, *99*, 1.
[24] P. V. Burmistrova, J. Maassen, T. Favaloro, B. Saha, S. Salamat, Y.R. Koh, M.S. Lundstrom, A. Shakouri, TD. Sands, *J. Appl. Phys.* **2013**, *113*, 153704.
[25] C. F. Johnston, M. A. Moram, M. J. Kappers, C. J. Humphreys, *Appl. Phys. Lett.* **2009**, *94*, 161109.
[26] M. A. Moram, C. F. Johnston, M. J. Kappers, C. J. Humphreys, *J. Cryst. Growth* **2009**, *311*, 3239.
[27] B. Saha, A. Shakouri, T. D. Sands, *Appl. Phys. Rev.* **2018**, *5*, 021101.
[28] B. Saha, G. V. Naik, S. Saber, C. Akatay, E. A. Stach, V. M. Shalaev, A. Boltasseva, T. D. Sands, *Phys. Rev. B* **2014**, *90*, 125420.
[29] B. Saha, S. Saber, G. V. Naik, A. Boltasseva, E. A. Stach, E. P. Kvam, T. D. Sands, *Phys. Status Solidi B* **2015**, *252*, 251.
[30] B. Saha, M. Garbrecht, J. A. Perez-Taborda, M. H. Fawey, Y. R. Koh, A. Shakouri, M. Martin-Gonzalez, L. Hultman, T. D. Sands, *Appl. Phys. Lett.* **2017**, *110*, 252104.
[31] B. Saha, J. A. Perez-Taborda, J. H. Bahk, Y. R. Koh, A. Shakouri, M. Martin-Gonzalez, T. D. Sands, *Phys. Rev. B* **2018**, *97*, 085301.
[32] S. Nayak, M. Baral, M. Gupta, J. Singh, M. Garbrecht, T. Ganguli, S. M. Shivaprasad, B. Saha, *Phys. Rev. B* **2019**, *99*, 161117.
[33] S. Kerdsongpanya, B. Alling, P. Eklund, *Phys. Rev. B* **2012**, *86*, 195140.
[34] M. Garbrecht, L. Hultman, M. H. Fawey, T. D. Sands, B. Saha, *Phys. Rev. Mater.* **2017**, *01*, 033402.
[35] G. Travaglini, F. Marabelli, R. Monnier, E. Kaldis, P. Wachter, *Phys. Rev. B* **1986**, *34*, 3876.
[36] B. Saha, J. Acharya, T. D. Sands, U. V. Waghmare, *J. Appl. Phys.* **2010**, *107*, 033715.
[37] T. R. Paudel, W. R. L. Lambrecht, *Phys. Rev. B* **2009**, *79*, 085205.
[38] B. Saha, G. Naik, V. P. Drachev, A. Boltasseva, E. E. Marinero, T. D. Sands, *J. Appl. Phys.* **2013**, *114*, 063519.
[39] H. Uchiyama, Y. Oshima, R. Patterson, S. Iwamoto, J. Shiomi, K. Shimamura, *Phys. Rev. Lett.* **2018**, *120*, 235901.
[40] U. Fano, *Phys. Rev.* **1961**, *124*, 1866.
[41] N. Tureson, M. Marteau, T. Cabioch, N. V. Nong, J. Jensen, J. Lu, G. Greczynski, D. Fournier, N. Singh, A. Soni, L. Belliard, P. Eklund, A. L. Febvrier, *Phys. Rev. B* **2018**, *98*, 205307.
[42] J. Lindhard, *K. Dan. Vidensk. Selsk., Mat.-Fys. Medd.* **1954**, *28*, 8.
[43] N. D. Mermin, *Phys. Rev. B* **1970**, *1*, 5.
[44] M. Chandrasekhar, J. B. Renucci, M. Cardona, *Phys. Rev. B* **1978**, *17*, 1623.
[45] D. Olego, M. Cardona, *Phys. Rev. B* **1981**, *23*, 6592.
[46] F. Cerdeira, T. A. Fjeldly, M. Cardona, *Phys. Rev. B* **1973**, *8*, 4734.